High-order finite-volume reconstruction on arbitrary unstructured grids

G.A. Gerolymos* and I. Vallet*
Corresponding author: isabelle.vallet@upmc.fr

* Université Pierre-et-Marie-Curie, 4 place Jussieu, 75005 Paris, France.

Abstract: We study scalable high-order least-squares reconstruction on arbitrary unstructured grids. We discuss in particular stencil construction and conditioning of the reconstruction procedure as a function of the degree of the reconstructing polynomial. The order-of-accuracy of the schemes is evaluated on different types of unstructured grids by calculating the error of the solution of the advection equation. Finally, we discuss the spectral accuracy of the reconstruction procedure.

Keywords: High-Order Schemes, Unstructured Meshes, Multidimensional Least-Squares Reconstruction, Advection Equation.

1 Introduction

Finite-volume methods are mathematically equivalent [1] to Petrov-Galerkin methods whose test space consists of piecewise constant functions. Several authors [1, 2, 3] have studied the influence of numerical grid on the accuracy of the reconstruction procedure, both concerning the choice between cell-centered and node-centered approaches, and various triangulations. Notice that the node-centered control-volumes are formed by joining together the centroids of all the cells having the node as vertex, *ie* the node-centered control-volumes are the dual-grid of the cell-centered mesh. This is analogous to the relation between Delaunay triangulations and Voronoi tesselations [4].

Therefore the relative advantages of cell-centered and node-centered finite-volume (FVs) schemes [1] are best understood, especially for high-order schemes, as the comparison of the relative performance of high-degree polynomial least-squares approximations [5] on different control volumes, relative to Delauney triangulations [4] or Voronoi tesselations [4] or some other connectivity between points [2]. We study in the present paper the performance of very-high-order least-squares reconstruction on different types of general regular polygonal grids.

2 Reconstruction of a scalar field

The reconstruction of the values of a scalar field from its cell-averages [6, 7, 8] is a particular case of the optimal recovery theory [1] where some property of an unknown function (feature operator) is sought from a set of (linear) functionals of the unknown function (information operator). Most finite volume methods are based on or are higher-order extensions of the basic least squares reconstruction procedure [3]. We formalize, in the following, polynomial least-squares (LSQ) reconstruction of a scalar field from the knowledge of its averages on general polygonal cells. We restrict the analysis to polygonal cells with straight edges, but it is straightforward to extend it to general curvilinear polygons (where the edges are smooth curves) using appropriate definitions of the Gauss integration points on the edges (quadrature of fluxes) and in the interior of the polygons (cubature to evaluate averages and moments [9, 10]). The grids considered are conformal, *ie* each edge is either a common edge of exactly 2 elements, or a boundary-edge [1]. Since the elements can
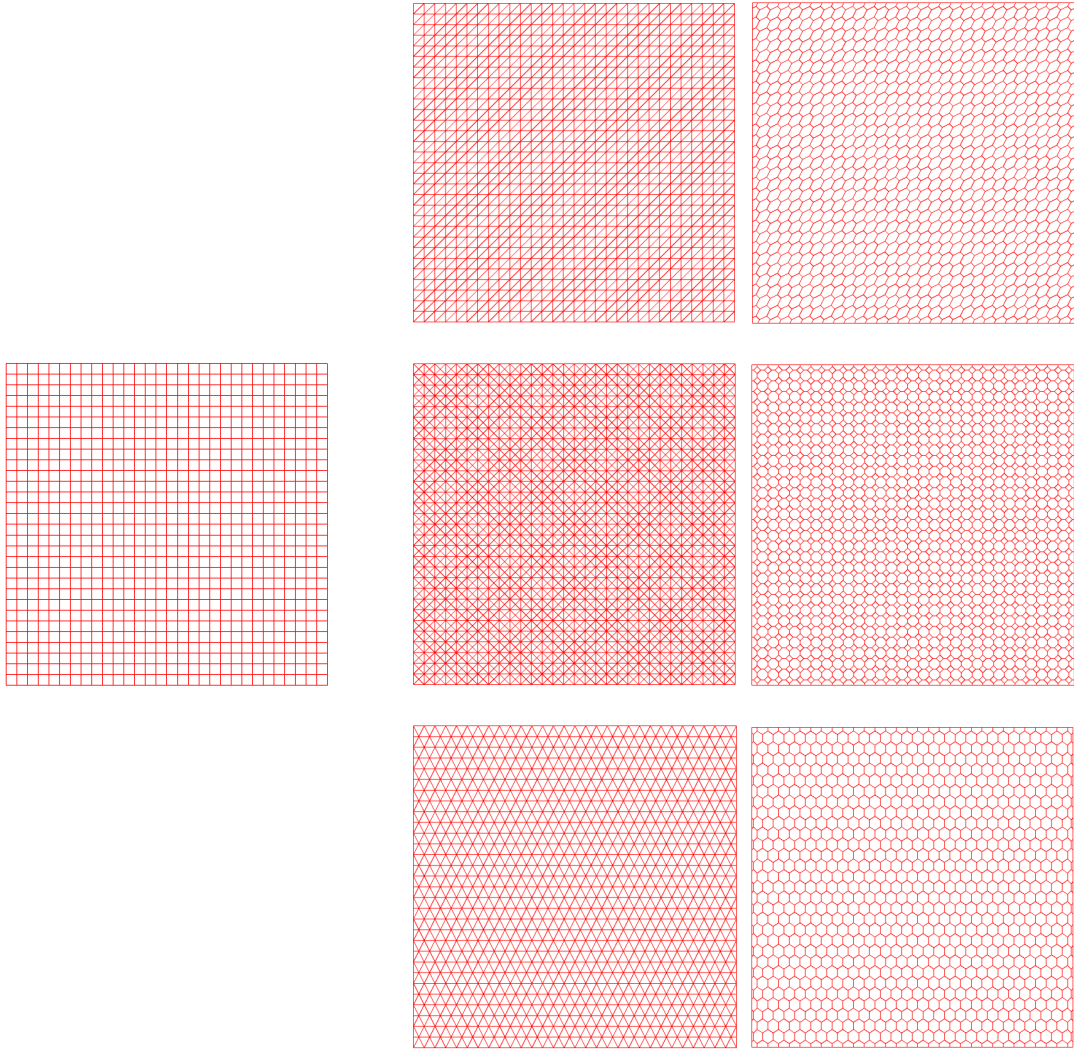
Figure 1: Examples of different triangular and general polygonal grids (dual to the triagular), obtained from a basic underlying Cartesian grid.

be arbitrary polygons, with different numbers of edges, all hanging nodes, eventually present in the grid, are eliminated by dividing the corresponding edge into 2 or more edges.

2.1 Basic mathematical tools

2.1.1 Polynomial $p(x,y) \in \mathbb{R}_{\mathrm{M}}[(x,y)]$

An algebraic polynomial of $(x,y) \in \mathbb{R}^2$, with real coefficients, of degree M reads

$$
\begin{aligned}
p(x,y) &= \sum_{m=0}^{M} \sum_{\ell=0}^{m} a_{\ell,m-\ell}\, x^{\ell} y^{m-\ell} \\
&= a_{0,0} + \sum_{m=1}^{M} \sum_{\ell=0}^{m} a_{\ell,m-\ell}\, x^{\ell} y^{m-\ell}
\end{aligned}
\tag{1}
$$

and has $\binom{M+2}{2}$ coefficients

$$
\underline{a}_{\mathrm{M}} := [\underbrace{a_{0,0}}_{n_c=1}, \cdots, \underbrace{a_{\ell,k}}_{n_c(\ell,k)}, \cdots, \underbrace{a_{0,\mathrm{M}]}}_{n_c=\binom{M+2}{2}}]^T
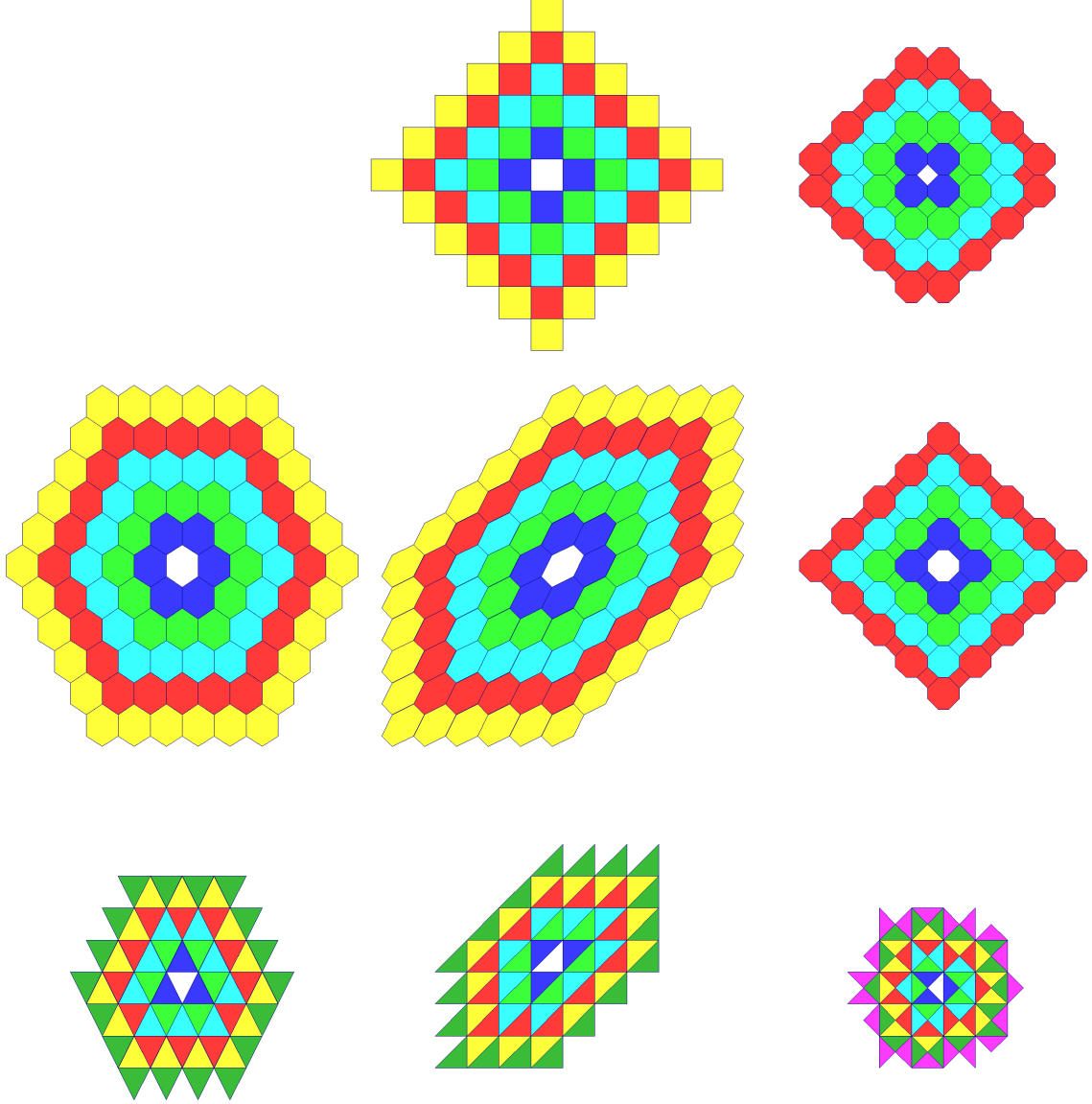\tag{2}
$$

Figure 2: Typical stencils, for the $M + 1 = 10$ LSQ reconstruction, for various computational grids (Fig. 1), constructed by adding successive levels of von Neumann neighbours to the previous level of the stencil (each colour corresponds to a level of neighbours).

where, for practical purposes, when building linear systems for the computation of the coefficients, we use instead the coefficient index

$$n_{\mathrm{c}}(\ell, k) := \binom{\ell + k + 1}{2} + k + 1 \ \in \{1, \cdots, \binom{M + 2}{2}\}$$
$$\ell, k \ \in \{0, \cdots, M\} \tag{3}$$

defining the row-index of the column-vector $\underline{a}_{\mathrm{M}}$ (eq. 2) corresponding to the coefficient $a_{\ell,k}$ of the powers $x^\ell y^{m-\ell}$ in (eq. 1). If a scalar field is reconstructed for a polynomial of degree M, then, provided all cubature and quadrature operations are exact for a polynomial of degree M, the resulting finite-volume method is $O(\Delta \ell^{\mathrm{M}+1})$, $\Delta \ell$ being a characteristic cell-size.

2.1.2 Quadrature and Cubature

The finite-volume reconstruction-based algorithm requires integration operations, both quadrature on the edges of an element (all elements considered in the present work are polygons with straight edges) and cubature on the surface of the element. In both cases we used Gauss-integration.

2.1.2.1 Quadrature For the computation of integrals on a segment, we used Gauss-Legendre quadrature, accurate to $O(\Delta \ell^{\mathrm{M}+1})$ (exact for polynomials of degree M)

$$\int_{P_1}^{P_2} f(x,y) = d\ell_{P_1 P_2} = |\vec{x}_2 - \vec{x}_1| \sum_{n_{\mathrm{c}}=1}^{\lfloor \frac{M}{2} \rfloor + 1} w_{n_{\mathrm{c}, \lfloor \frac{M}{2} \rfloor + 1}} f(x_{n_{\mathrm{c}_{P_1 P_2}}}, y_{n_{\mathrm{c}_{P_1 P_2}}}) + O(\Delta \ell^{\mathrm{M}+1}) \tag{4}$$

where $P_1 P_2$ is the segment defined by the distinc points $p_1 = (x_1, y_1)$ and $p_2 = (x_2, y_2)$ and $w_{n_{\mathrm{c}}}$ are the weights corresponding to the Gauss-Legendre quadrature points on $p_1 p_2$

$$w_{n_{\mathrm{c}, \mathrm{N}}} = \frac{1}{2} \breve{w}_{\mathrm{GL}}(n_{\mathrm{G}}, N) \tag{5}$$

$$\vec{x}_{n_{\mathrm{c}_{p_1 p_2}}} = \vec{x}_1 + \frac{1}{2} \zeta(n_{\mathrm{G}}, N)(\vec{x}_2 - \vec{x}_1) \tag{6}$$

The weights and locations of the Gauss-Legendre quadrature points are available in many textbooks, and can be easily computed using symbolic calculation. They were tabulated for completeness (Tab. 1) with 69-digit accuracy (when simple analytical expressions were not available).

Notice that, for nonlinear conservation laws, the Gauss points on the edge of an element determine the points where the exact or approximate Riemann solver is applied so that the Gauss-Legendre points, which are symmetrically distributed around the edge-midpoint and do not contain the edges, are a good choice.

2.1.2.2 Cubature Cubature (surface integration) is necessary to determine the relation between the coefficients of the reconstructing polynomial and its cell-averages. Therefore, as long as the cubature used is exact for the chosen degree M of the reconstructing polynomial (which determines the order-of-accuracy of the scheme, the particular Gauss cubature used has no influence on the solution.

In the present computations, we used the cubature locations and weights defined by Dunavant [11], following the moments approach of Cowper [12]. For a triangular element $\Omega_\Delta := \Delta_{P_1 P_2 P_3}$

$$\int \int_{\Omega_\Delta} f(x,y) dx dy = A_{\Omega_\Delta} \sum_{n_{\mathrm{c}}=1}^{N_{\mathrm{G}_\mathrm{M}}} f(x_{n_{\mathrm{c,M}}}, y_{n_{\mathrm{c,M}}}) w_{n_{\mathrm{c,M}}} \tag{7}$$

where

$$\vec{x}_{n_{\mathrm{c,M}}} = c_{1_{n_{\mathrm{c,M}}}} \vec{x}_1 + c_{2_{n_{\mathrm{c,M}}}} \vec{x}_2 + c_{3_{n_{\mathrm{c,M}}}} \vec{x}_3 \tag{8}$$

are the Gauss points providing exact cubature on the triangle for polynomials of degree $\leq M$, with $w_{n_{\mathrm{c,M}}}$ the corresponding weights and $c_{1_{n_{\mathrm{c,M}}}}$, $c_{2_{n_{\mathrm{c,M}}}}$, $c_{3_{n_{\mathrm{c,M}}}}$ the corresponding barycentric coordinates (these were tabulated up to $M = 20$ by Dunavant [11]). The cubature rules for some $M \in \{1, 20\}$ given in [11] include some cases with negative weights (N[11]) or with Gauss points outside of the triangle (O[11]). In the present work, these rules ($M \in \{3, 7, 11, 15, 16, 18\}$) were replaced by the higher-order rules ($M \in \{4, 8, 12, 17, 17, 19\}$ respectively). This gives fully symmetric (in barycentric coordinates) and PI (positive weights and Gauss points inside the triangle [11]) rules up to $M = 19$, which corresponds to the $O(\Delta \ell^{20})$ scheme. Notice, that such symmetric PI rules for cubature on the triangle can also be used for face-integration in the 3-D extension of the method.

n	m	$x_{\mathrm{LEG}_{nm}}$	$w_{\mathrm{GAUSLEG}_{nm}}$
1	1	0	2
2	1	$-\frac{1}{\sqrt{3}}$	1
	2	$+\frac{1}{\sqrt{3}}$	1
3	1	$-\frac{\sqrt{3}}{\sqrt{5}}$	$\frac{5}{9}$
	2	0	$\frac{8}{9}$
	3	$+\frac{\sqrt{3}}{\sqrt{5}}$	$\frac{5}{9}$
4	1	$-\frac{\sqrt{15+2\sqrt{30}}}{\sqrt{35}}$	$\frac{49}{6(18+\sqrt{30})}$
	2	$-\frac{\sqrt{15-2\sqrt{30}}}{\sqrt{35}}$	$\frac{49}{6(18-\sqrt{30})}$
	3	$+\frac{\sqrt{15-2\sqrt{30}}}{\sqrt{35}}$	$\frac{49}{6(18-\sqrt{30})}$
	4	$+\frac{\sqrt{15+2\sqrt{30}}}{\sqrt{35}}$	$\frac{49}{6(18+\sqrt{30})}$
5	1	$-\frac{\sqrt{35+2\sqrt{70}}}{3\sqrt{7}}$	$\frac{5103}{50(322+13\sqrt{70})}$
	2	$-\frac{\sqrt{35-2\sqrt{70}}}{3\sqrt{7}}$	$\frac{5103}{50(322-13\sqrt{70})}$
	3	0	$\frac{128}{225}$
	2	$+\frac{\sqrt{35-2\sqrt{70}}}{3\sqrt{7}}$	$\frac{5103}{50(322-13\sqrt{70})}$
	5	$+\frac{\sqrt{35+2\sqrt{70}}}{3\sqrt{7}}$	$\frac{5103}{50(322+13\sqrt{70})}$
6	1	$-0.9324695142031520278123015544939946091347657377122898248725496165266 13\ldots$	$0.1713244923791703450402961421727328935268225014840439823986354397989 45\ldots$
	2	$-0.6612093864662645136613995950199053470064485643951700708145267058521 83\ldots$	$0.3607615730481386075698335138377161116615218927467454822897392402371 40\ldots$
	3	$-0.2386191860831969086305017216807119354186106301400213501813951645742 74\ldots$	$0.4679139345726910473898703439895509948116556057692105353116253199639 14\ldots$
	4	$+0.2386191860831969086305017216807119354186106301400213501813951645742 74\ldots$	$0.4679139345726910473898703439895509948116556057692105353116253199639 14\ldots$
	5	$+0.6612093864662645136613995950199053470064485643951700708145267058521 83\ldots$	$0.3607615730481386075698335138377161116615218927467454822897392402371 40\ldots$
	6	$+0.9324695142031520278123015544939946091347657377122898248725496165266 13\ldots$	$0.1713244923791703450402961421727328935268225014840439823986354397989 45\ldots$
7	1	$-0.9491079123427585245261896840478512624007709376706177835487691039130 63\ldots$	$0.1294849661688696932706114326790820183285874022599466639772086387246 55\ldots$
	2	$-0.7415311855993944398636478732807884070741476471413902601199553519674 29\ldots$	$0.2797053914892766679014677714237958248692506522659876453701403269361 8\ldots$
	3	$-0.4058451513773971669066064120769614633473820140993701263870432517946 63\ldots$	$0.3818300505051189449503697754889751338783650835338627347510834510307 05\ldots$
	4	0	$0.4179591836734693877551020408163265306122448979591836734693877551020 40\ldots$
	5	$+0.4058451513773971669066064120769614633473820140993701263870432517946 63\ldots$	$0.3818300505051189449503697754889751338783650835338627347510834510307 05\ldots$
	6	$+0.7415311855993944398636478732807884070741476471413902601199553519674 29\ldots$	$0.2797053914892766679014677714237958248692506522659876453701403269361 8\ldots$
	7	$+0.9491079123427585245261896840478512624007709376706177835487691039130 63\ldots$	$0.1294849661688696932706114326790820183285874022599466639772086387246 55\ldots$
8	1	$-0.9602898564975362316835608685694729904282352343014520382716397773724 24\ldots$	$0.1012285362903762591525313543099621901153940910516849570590036980647 40\ldots$
	2	$-0.7966664774136267395915539364758304368371173161596483207017029503921 7\ldots$	$0.2223810344533744705443559944262408844301308700512495647259092892936 16\ldots$
	3	$-0.5255324099163289858177390491892463490419642431203928577508570992722 454\ldots$	$0.3137066458778872873379622019866013132603289990027349376902639450746 56\ldots$
	4	$-0.1834346424956498049394761423600183980665675781291297378231718847369 9204\ldots$	$0.3626837833783619829651504492771956121941460398943305405248230675666 86\ldots$
	5	$+0.1834346424956498049394761423600183980665675781291297378231718847369 9204\ldots$	$0.3626837833783619829651504492771956121941460398943305405248230675666 86\ldots$
	6	$+0.5255324099163289858177390491892463490419642431203928577508570992722 454\ldots$	$0.3137066458778872873379622019866013132603289990027349376902639450749 56\ldots$
	7	$+0.7966664774136267395915539364758304368371173161596483207017029503921 7\ldots$	$0.2223810344533744705443559944262408844301308700512495647259092892936 16\ldots$
	8	$+0.9602898564975362316835608685694729904282352343014520382716397773724 24\ldots$	$0.1012285362903762591525313543099621901153940910516849570590036980647 40\ldots$

Table 1: Roots $x_{\mathrm{LEG}_{nm}}$ of Legendre polynomials $p_{\mathrm{LEG},n}(x)$ for $n \in \{1, \cdots, 8\}$, and associated weights $w_{\mathrm{GAUSLEG}_{nm}}$ for Gauss-Legendre quadrature.

Finally, in the case of polygonal elements Ω, we may simply split the elements into triangle defined by the centroid of the polygone and each edge

$$\Omega = \bigcup_{n_{\mathrm{edge}}=1}^{N_{\mathrm{edge}}} \Delta_{\mathrm{BC},n_{\mathrm{edge}}} \tag{9}$$

and apply the rules (eq. 7) for each triangle

$$\int\int_{\Omega} f(x,y)dxdy \;\; = \;\; \sum_{n_{\mathrm{edge}}=1}^{N_{\mathrm{edge}_{\Omega}}} \int\int_{\Delta_{\mathrm{BC},n_{\mathrm{edge}}}} f(x,y)dxdy \tag{10}$$

$$= \;\; A_{\Omega}\sum_{n_{\mathrm{C}}=1}^{N_{\mathrm{C}_{\Omega}}} f(x_{n_{\mathrm{C}_{\Omega}}},y_{n_{\mathrm{C}_{\Omega}}})w_{n_{\mathrm{C}_{\Omega}}} \tag{11}$$

where the weights for the integration on the polygons are readily assembled from the cubature rules on each triangle.

Notice that, for the 2-D case studied here, the cubature operation is only required to compute the least-squares matrix, whose inversion determines the coefficients of the reconstructing polynomial, so that, if the grid is fixed in time, the cubature cost is not relevant.

2.1.3 Least squares reconstruction

Reconstruction [7] consists in approximating a function $u(x,y)$ from information concerning the values of a (linear) functional of u at several distinct locations. In the finite-volume case (Petrov-Galerkin finite-elements with constant test functions [1]) the functional is the cell-average of $u(x,y)$ on the element Ω_n

$$\bar{u}_{\Omega_n} := \frac{1}{A_{\Omega_n}}\int\int_{\Omega_n} u(x,y)dxdy \tag{12}$$

Given a stencil around the element Ω_n,

$$\mathrm{S}_n := \{\Omega_n\}\bigcup \mathrm{S}_{ngb_n} \tag{13}$$

$$\mathrm{S}_{ngb_n} := \{\Omega_{ngb_1},\cdots,\Omega_{ngb_{N_{ngb_n}}}\} \tag{14}$$

containing the element and N_{ngb_n} neighbours, the reconstruction problem approximates $u(x,y)$ from the values of the averages $\{\bar{u}_m; m \in \mathrm{S}_{ngb}\}$ of the elements in the stencil. In the least-squares approach of [5] which is widely used the approximating (reconstructing) polynomial $p_{\mathrm{R},\mathrm{M},\mathrm{S}_n}(x,y)$ satisfies exactly the value of the average $\bar{u}_n$ in the cell n, and in a least-squares sense the value of the average on the other cells of the stencil

$$\frac{1}{A_{\Omega_n}}\int\int_{\Omega_n} p_{\mathrm{R},\mathrm{M},\mathrm{S}_n}(x,y)dxdy = \bar{u}_{\Omega_n} \tag{15}$$

$$\frac{\partial J_{\mathrm{LSQ},\mathrm{R},\mathrm{M},\mathrm{S}_n}}{\partial a_{\mathrm{R},\mathrm{M},\mathrm{S}_n,\ell,k}} = 0 \;\; \forall \ell,k \in \{0,\cdots,M\} : \ell+k \leq M \tag{16}$$

$$J_{\mathrm{LSQ},\mathrm{R},\mathrm{M},\mathrm{S}_n} := \sum_{m\in\mathrm{S}_{ngb_n}} w^2_{\mathrm{LSQ}_{\Omega_m,\Omega_n}} \left[\frac{1}{A_{\Omega_m}}\int\int_{\Omega_m} p_{\mathrm{R},\mathrm{M},\mathrm{S}_n}(x,y)dxdy - \bar{u}_{\Omega_m}\right]^2 \tag{17}$$

Many authors use distance weighting. In the present paper, we used unweighted least-squares

$$w_{\mathrm{LSQ}_{\Omega_m,\Omega_n}} := 1 \tag{18}$$

3 Results

As an example, consider linear (in the sense of Godunov's theorem [13]) least-squares schemes [5] for the 2-D advection equation on a square domain (Fig. 1). The points of a regular Cartesian grid can be triangulated in different ways (Fig. 1), and the dual-grids composed by the control-volumes constructed by joining the barycenters of the cells around each vertex are general polygonal grids (Fig. 1), while the dual of a basic quasi-Delauney triangulation with equilateral triangles is a quasi-Voronoi tesselation of the square (Fig. 1).

The stencil was constructed using successive levels of neighbours (Fig. 2). Level $\ell_{\text{NGB}} = 1$ consists of the edge-neighbours (von Neumann neighbours) of the element (Fig. 2). For any given level $\ell_{\text{NGB}} \in \{1, \cdots, L_{\text{NGB}}\}$ of stencil construction, the next level $\ell_{\text{NGB}} + 1$ is constructed by adding the edge-neighbours of the elements belonging to the ℓ_{NGB}-level (Fig. 2). The minimum requirement is that the number of neighbours

$$N_{\text{NGB}} \geq \binom{M+1}{2} - 1 \tag{19}$$

be larger than the coefficients of the polynomial. This necessary condition is not always sufficient, because in some instances the reconstruction matrix A_{LSQ} is singular. For all the cases studied ($M \leq 9$), when A_{LSQ} was found singular, adding one more level of neighbours suffices to solve the problem.

Comparison of the numerical solution of the 2-D advection equation with the analytical solution, on progressively refined grids of each type (Figs. 3-9), indicates that $O(\Delta\ell^{M+1})$-accuracy is always obtained for polynomial reconstruction of degree M. Accuracy for a given level of grid refinement, is higher when the number of neighbours is closest to the equality in (eq. 19).

In order to compare the performance of different grids, as they are progressively refined, a common measure of grid-size is required. Often, when considering triangular grids, the triangle diameter (circumradius) is used. Nonetheless, for irregular polygons, the extension of this definition is not unique, and, *eg*, defining the cell-size as the largest circumradius of all triangles constructed from any possible triplet of the vertices of the polygon may yield very large values for skew cells (Fig. 9). For this reason, it was prefered to define the size of polygon Ω_n, with vertices $V_{\Omega_n} := \{\vec{x}_1, \cdots, \vec{x}_{N_{\Omega_n}}\}$ as the maximum Euclidian distance between 2 vertices

$$\Delta\ell_{\Omega_n} := \max_{\substack{\vec{x}_\ell \in V_{\Omega_n} \\ \vec{x}_m \in V_{\Omega_n}}} ||\vec{x}_\ell - \vec{x}_m||_2 \tag{20}$$

and the representative grid-size as the maximum cell-size

$$\Delta\ell_{\mathcal{G}} = \max_{p_n \in \mathcal{G}} \Delta\ell_{\Omega_n} \tag{21}$$

Plotting the error for the advection problem as a function of $\Delta\ell$, for the various grids studied, provides consistant results between various grids (Fig. 10). Notice that the finite-volume LSQ-reconstruction results on the Cartesian grid, are very close to the upwind-biased finite-difference computations [14] on the same grid (Fig. 10).

As the order of accuracy $M+1$ increases, the condition number of A_{LSQ} increases, roughly as $\text{cond}_\infty A_{\text{LSQ}} \sim 10^{2(M-\frac{3}{2})}$ (Fig. 11). Notice that $\text{cond}_\infty A_{\text{LSQ}}$ for the quasi-equilateral triangles grid is substantially lower (better conditioning) compared to the other grids, as $M + 1$ increases.
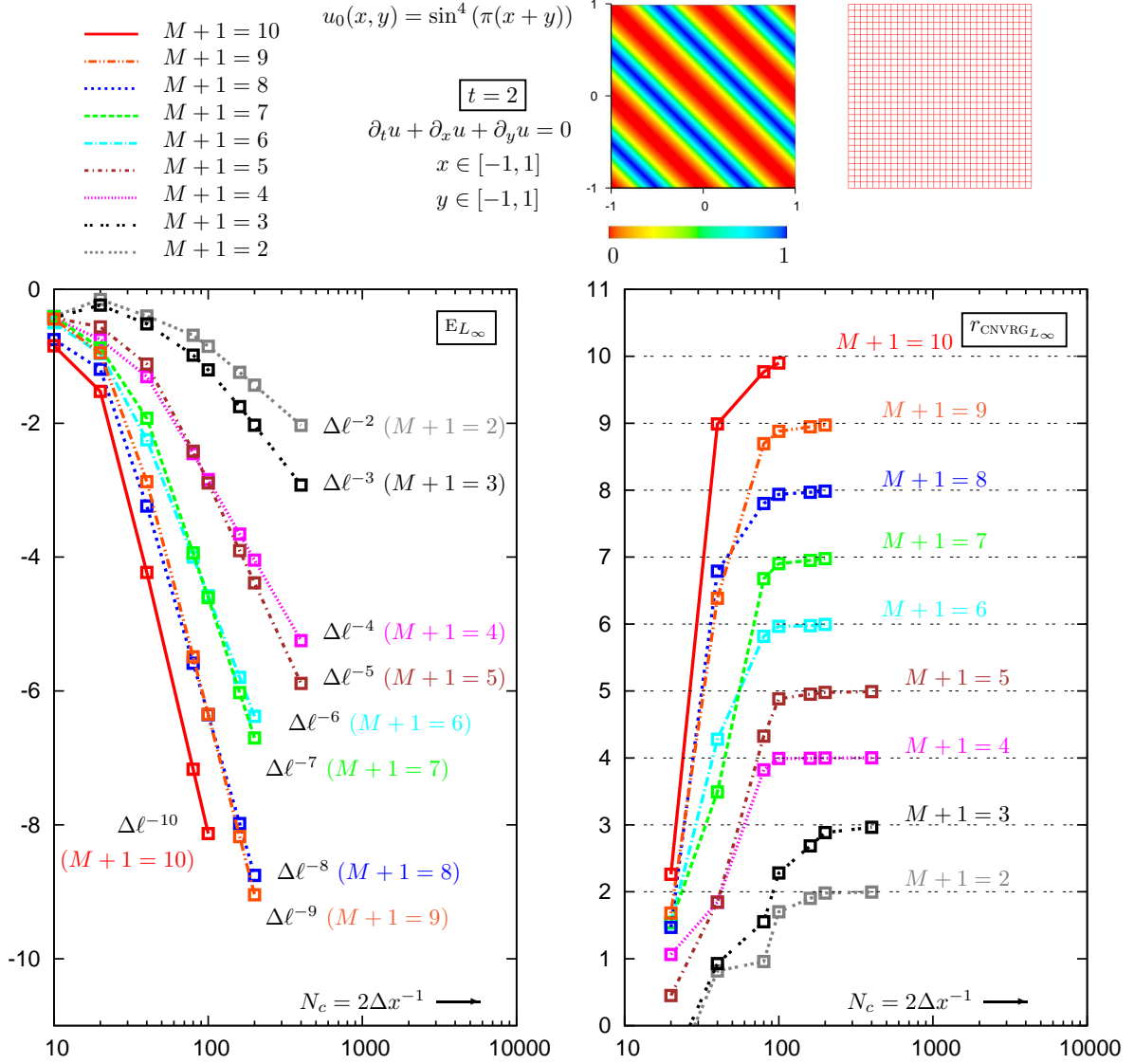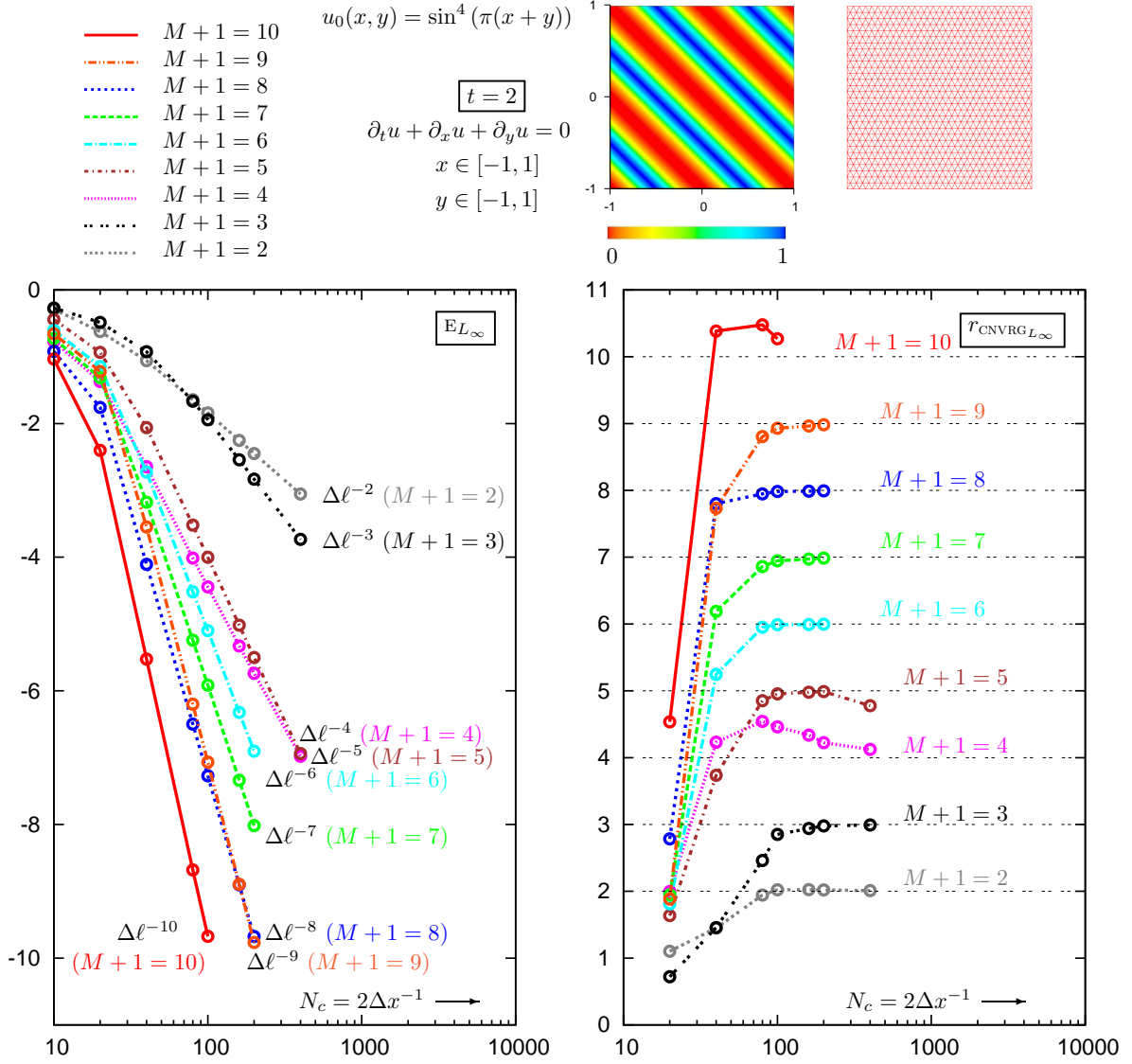
Figure 3: L_∞-norm error E_{L_∞} and rate-of-convergence $r_{\mathrm{CNVRG}_{L_\infty}}$, as a function of the number of grid-cells $N_c = N_i - 1 = N_j - 1$ of the underlying Cartesian grid, for the difference from the analytical solution of numerical computations of for the 2-D linear advection equation $\partial_t + \partial_x u + \partial_y u = 0$ ($x \in [-1, 1]$, $y \in [-1, 1]$), with periodic BCs, and IC $u_0(x) = \sin(\pi(x + y))$, using LSQ reconstruction, on a Cartesian finite-volume grid, for various orders $M + 1 \in \{2, \cdots, 10\}$, and $\ell \mathrm{SSPRK}(M + 2, M + 1)$ time-integration [15] with CFL $= \Delta t \Delta x_{\mathrm{CRTSN}}^{-1} = \Delta t \Delta y_{\mathrm{CRTSN}}^{-1} = \frac{2}{10}$, on progressively refined computational grids.
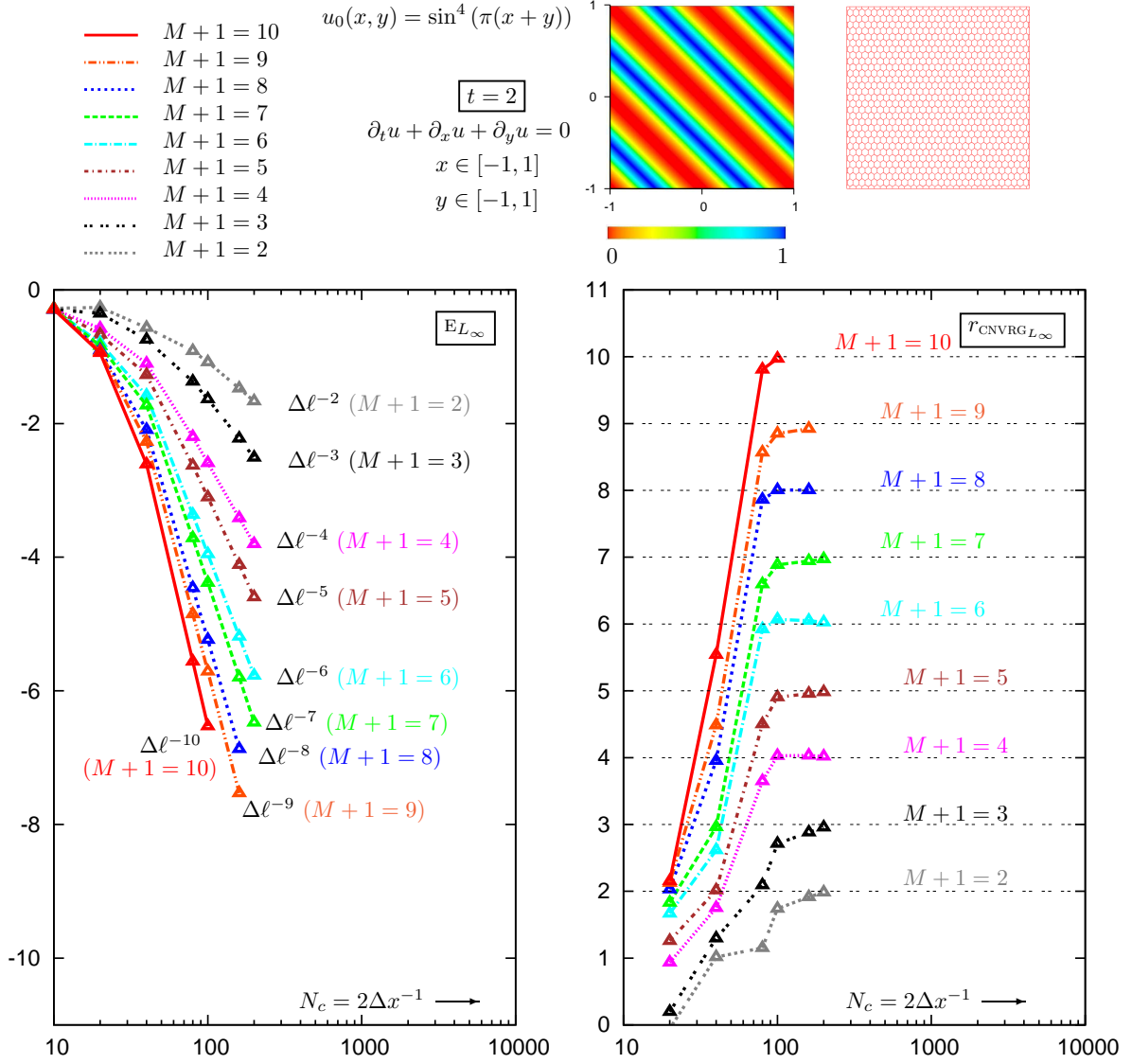
Figure 4: L_∞-norm error E_{L_∞} and rate-of-convergence $r_{\mathrm{CNVRG}_{L_\infty}}$, as a function of the number of grid-cells $N_c = N_i - 1 = N_j - 1$ of the underlying Cartesian grid, for the difference from the analytical solution of numerical computations of the advection equation, for the 2-D linear advection equation $\partial_t + \partial_x u + \partial_y u = 0$ ($x \in [-1, 1]$, $y \in [-1, 1]$), with periodic BCs, and IC $u_0(x) = \sin(\pi(x + y))$, using LSQ reconstruction, on a finite-volume grid of near-equilateral triangles (type III of [2]), for various orders $M + 1 \in \{2, \cdots, 10\}$, and ℓSSPRK$(M + 2, M + 1)$ time-integration [15] with CFL $= \Delta t \Delta x_{\mathrm{CRTSN}}^{-1} = \Delta t \Delta y_{\mathrm{CRTSN}}^{-1} = \frac{2}{10}$, on progressively refined computational grids.
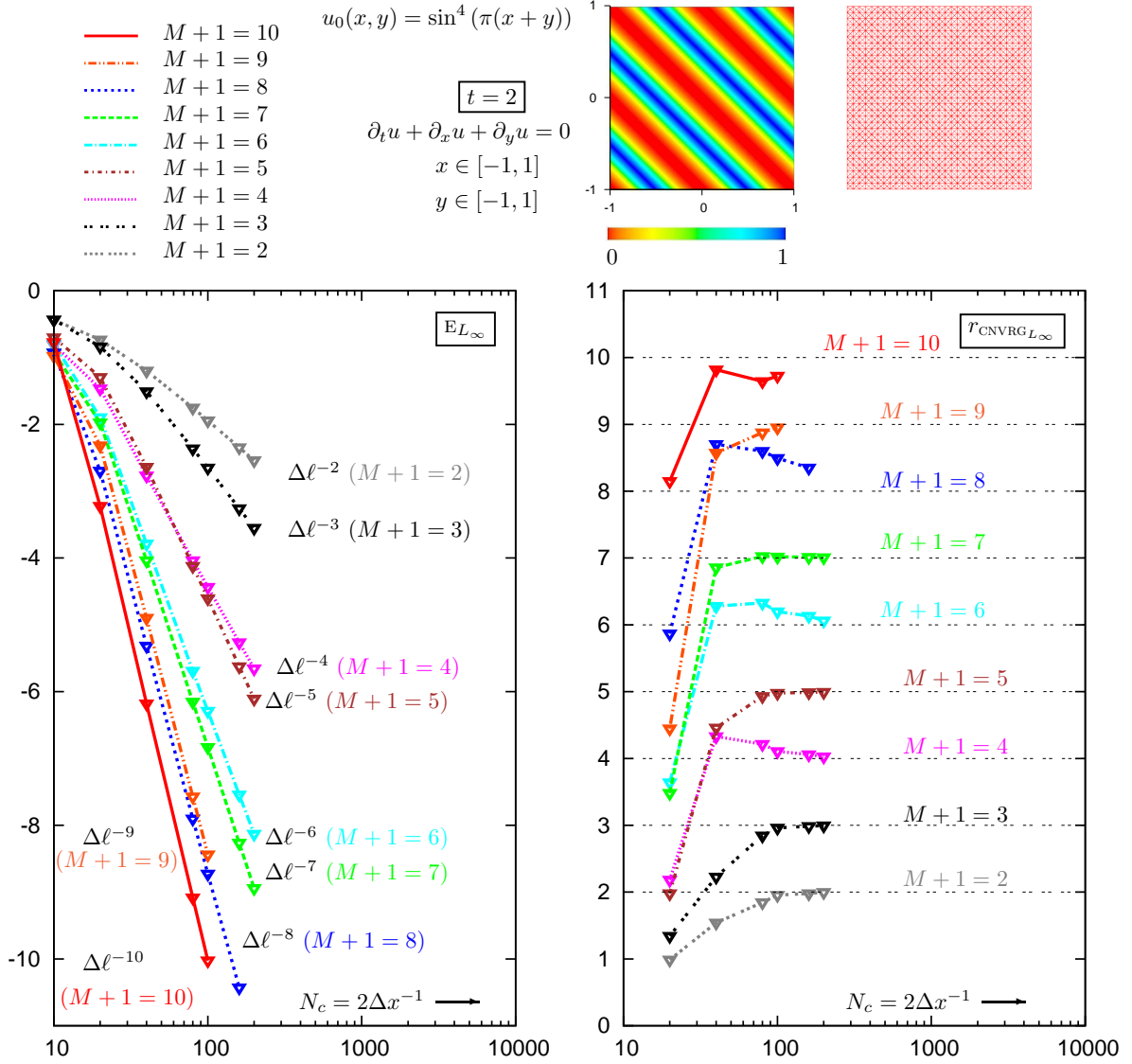
Figure 5: L_∞-norm error E_{L_∞} and rate-of-convergence $r_{\mathrm{CNVRG}_{L_\infty}}$, as a function of the number of grid-cells $N_c = N_i - 1 = N_j - 1$ of the underlying Cartesian grid, for the difference from the analytical solution of numerical computations of the advection equation, for the 2-D linear advection equation $\partial_t + \partial_x u + \partial_y u = 0$ ($x \in [-1, 1]$, $y \in [-1, 1]$), with periodic BCs, and IC $u_0(x) = \sin(\pi(x + y))$, using LSQ reconstruction, on the finite-volume dual grid of the near-equilateral triangles mesh (Fig. 4), for various orders $M + 1 \in \{2, \cdots, 10\}$, and ℓSSPRK$(M + 2, M + 1)$ time-integration [15] with CFL $= \Delta t \Delta x^{-1}_{\mathrm{CRTSN}} = \Delta t \Delta y^{-1}_{\mathrm{CRTSN}} = \frac{2}{10}$, on progressively refined computational grids.

Figure 6: L_∞-norm error E_{L_∞} and rate-of-convergence $r_{\mathrm{CNVRG}_{L_\infty}}$, as a function of the number of grid-cells $N_c = N_i - 1 = N_j - 1$ of the underlying Cartesian grid, for the difference from the analytical solution of numerical computations of the advection equation, for the 2-D linear advection equation $\partial_t + \partial_x u + \partial_y u = 0$ ($x \in [-1,1]$, $y \in [-1,1]$), with periodic BCs, and IC $u_0(x) = \sin(\pi(x + y))$, using LSQ reconstruction, on a finite-volume grid of cross-orthogonal triangles obtained by destructuring a Cartesian mesh (type II of [2]), for various orders $M + 1 \in \{2, \cdots, 10\}$, and ℓSSPRK$(M + 2, M + 1)$ time-integration [15] with CFL $= \Delta t \Delta x_{\mathrm{CRTSN}}^{-1} = \Delta t \Delta y_{\mathrm{CRTSN}}^{-1} = \frac{2}{10}$, on progressively refined computational grids.
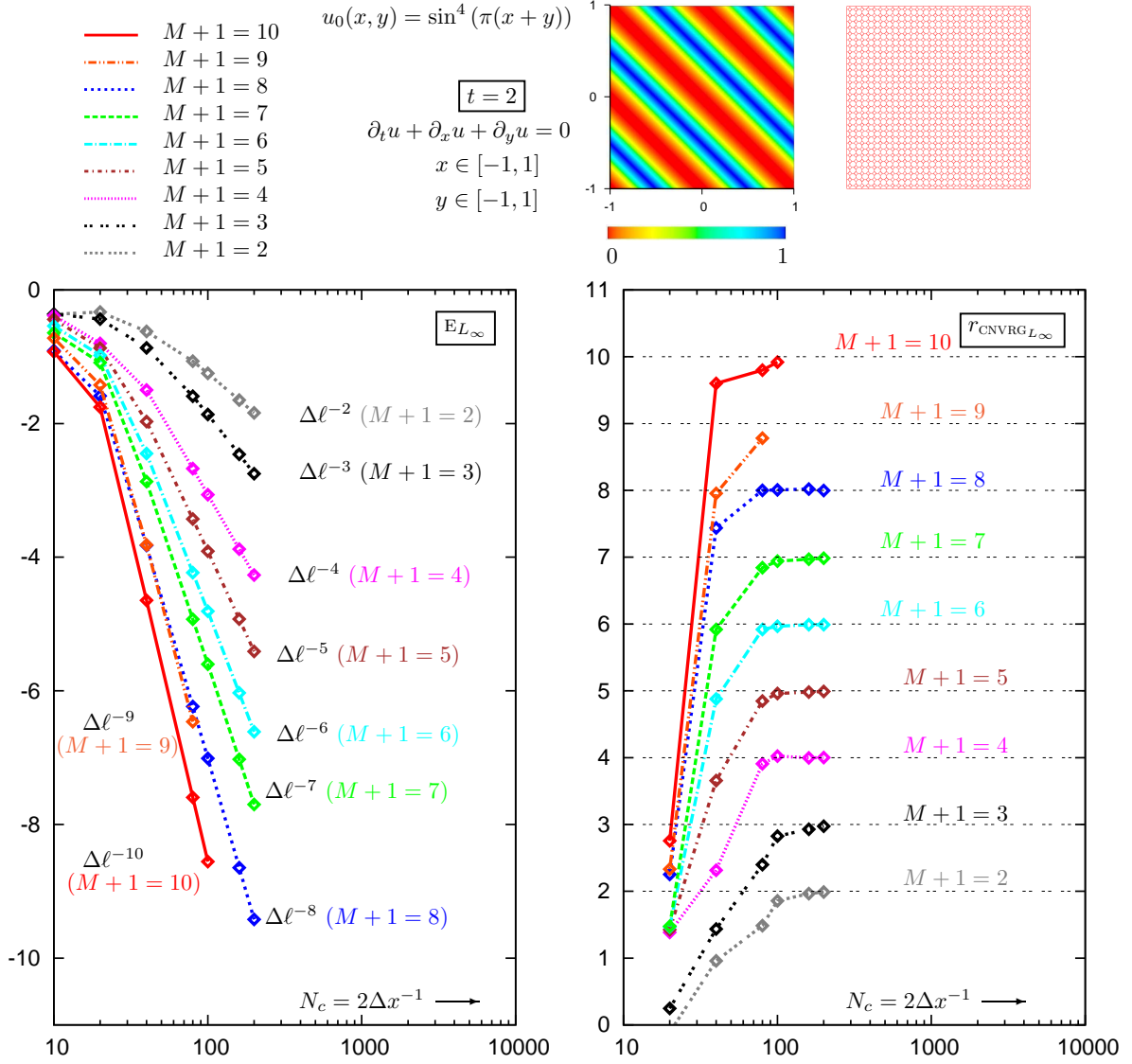
Figure 7: L_∞-norm error E_{L_∞} and rate-of-convergence $r_{\mathrm{CNVRG}_{L_\infty}}$, as a function of the number of grid-cells $N_c = N_i - 1 = N_j - 1$ of the underlying Cartesian grid, for the difference from the analytical solution of numerical computations of the advection equation, for the 2-D linear advection equation $\partial_t + \partial_x u + \partial_y u = 0$ ($x \in [-1, 1]$, $y \in [-1, 1]$), with periodic BCs, and IC $u_0(x) = \sin(\pi(x + y))$, using LSQ reconstruction, on the finite-volume dual grid of the cross-orthogonal triangles mesh (Fig. 6), for various orders $M + 1 \in \{2, \cdots, 10\}$, and ℓSSPRK($M + 2, M + 1$) time-integration [15] with CFL $= \Delta t \Delta x_{\mathrm{CRTSN}}^{-1} = \Delta t \Delta y_{\mathrm{CRTSN}}^{-1} = \frac{2}{10}$, on progressively refined computational grids.
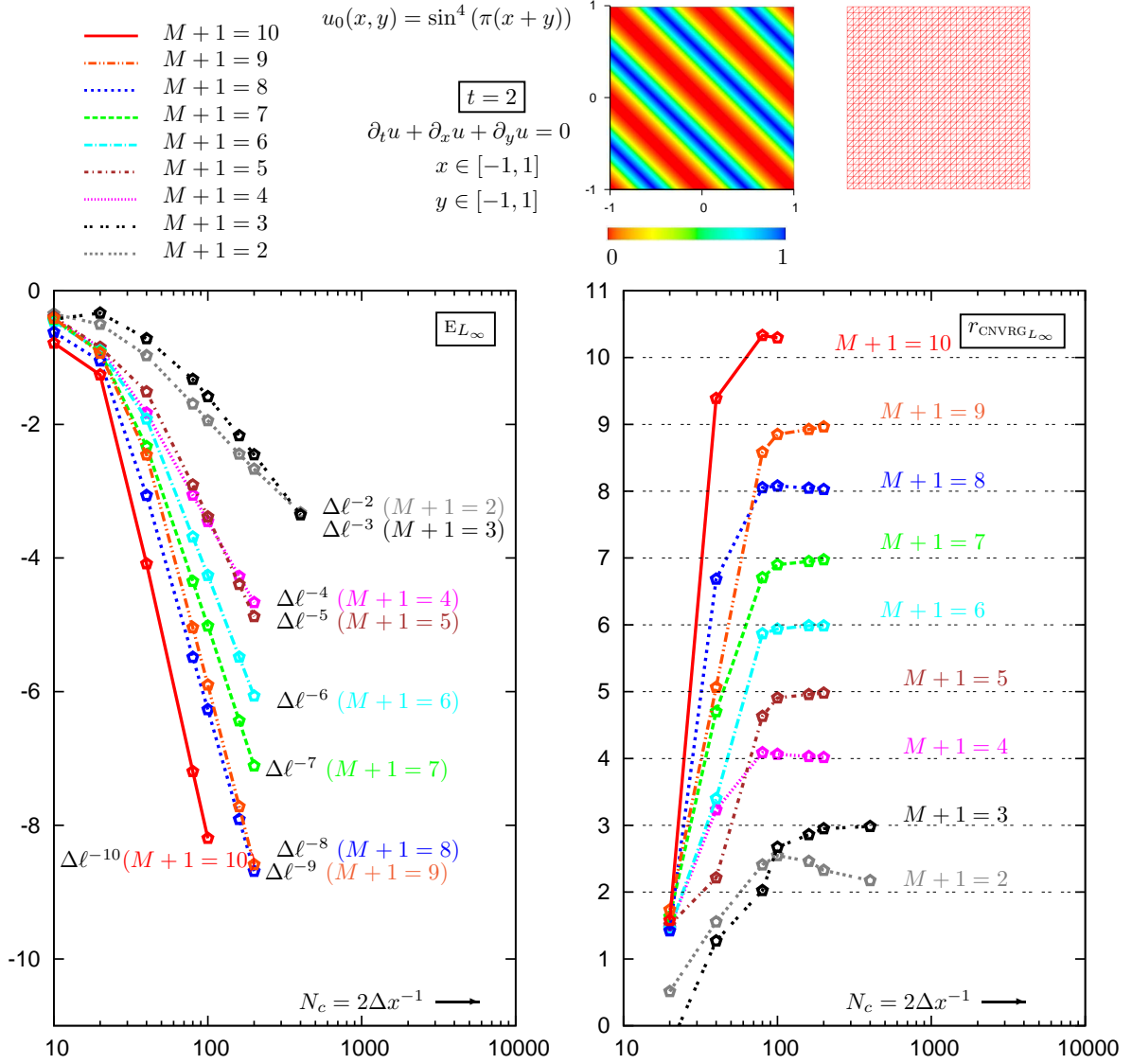
Figure 8: L_∞-norm error E_{L_∞} and rate-of-convergence $r_{\mathrm{CNVRG}_{L_\infty}}$, as a function of the number of grid-cells $N_c = N_i - 1 = N_j - 1$ of the underlying Cartesian grid, for the difference from the analytical solution of numerical computations of the advection equation, for the 2-D linear advection equation $\partial_t + \partial_x u + \partial_y u = 0$ ($x \in [-1, 1]$, $y \in [-1, 1]$), with periodic BCs, and IC $u_0(x) = \sin(\pi(x + y))$, using LSQ reconstruction, on a finite-volume grid of orthogonal triangles obtained by destructuring a Cartesian mesh (type III of [2]), for various orders $M + 1 \in \{2, \cdots, 10\}$, and $\ell \mathrm{SSPRK}(M+2, M+1)$ time-integration [15] with CFL $= \Delta t \Delta x_{\mathrm{CRTSN}}^{-1} = \Delta t \Delta y_{\mathrm{CRTSN}}^{-1} = \frac{2}{10}$, on progressively refined computational grids.
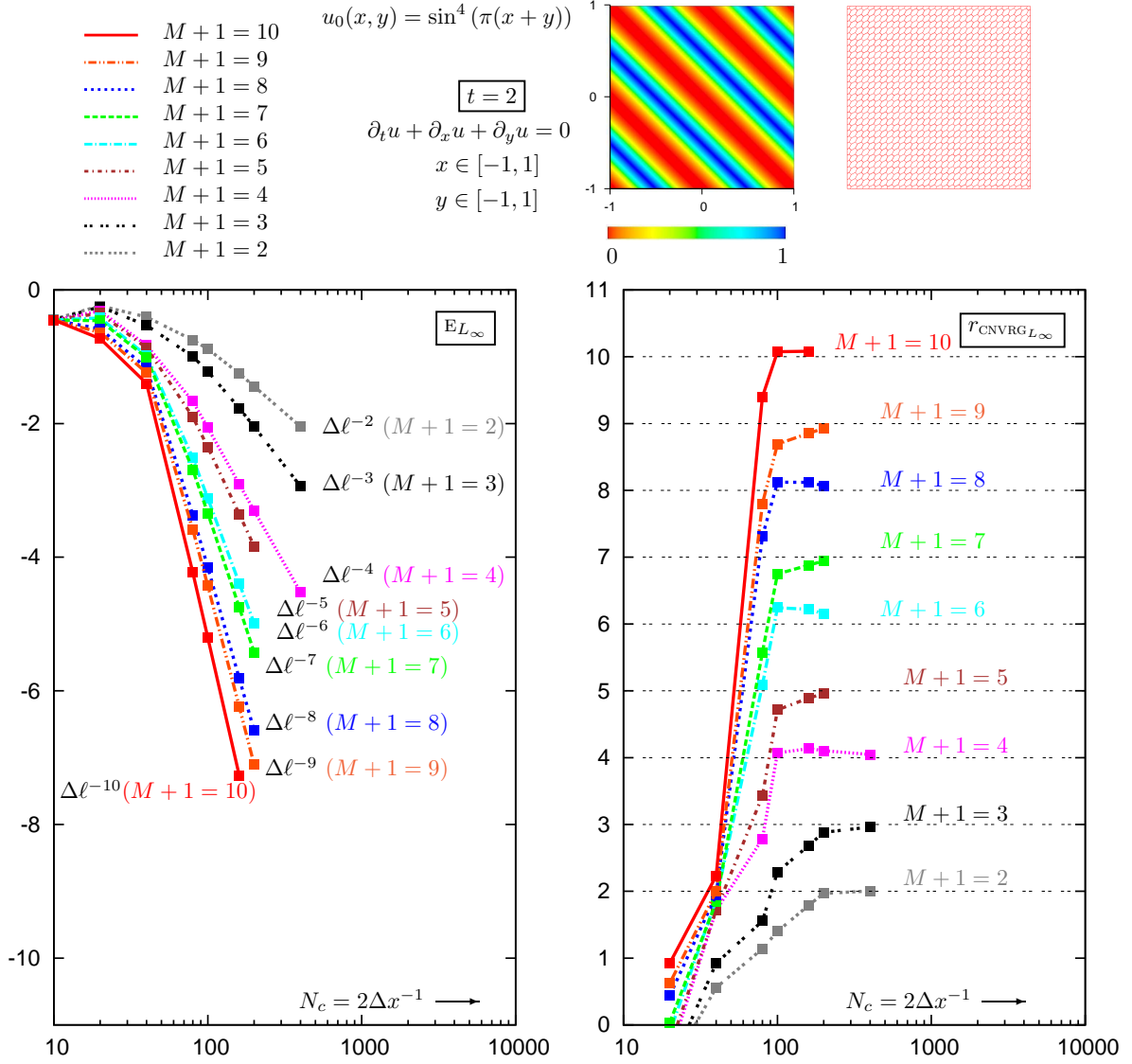
Figure 9: L_∞-norm error E_{L_∞} and rate-of-convergence $r_{\mathrm{CNVRG}_{L_\infty}}$, as a function of the number of grid-cells $N_c = N_i - 1 = N_j - 1$ of the underlying Cartesian grid, for the difference from the analytical solution of numerical computations of the advection equation, for the 2-D linear advection equation $\partial_t + \partial_x u + \partial_y u = 0$ ($x \in [-1, 1]$, $y \in [-1, 1]$), with periodic BCs, and IC $u_0(x) = \sin(\pi(x + y))$, using LSQ reconstruction, on the finite-volume dual grid of the orthogonal triangles mesh (Fig. 8), for various orders $M + 1 \in \{2, \cdots, 10\}$, and $\ell\mathrm{SSPRK}(M + 2, M + 1)$ time-integration [15] with CFL $= \Delta t \Delta x_{\mathrm{CRTSN}}^{-1} = \Delta t \Delta y_{\mathrm{CRTSN}}^{-1} = \frac{2}{10}$, on progressively refined computational grids.
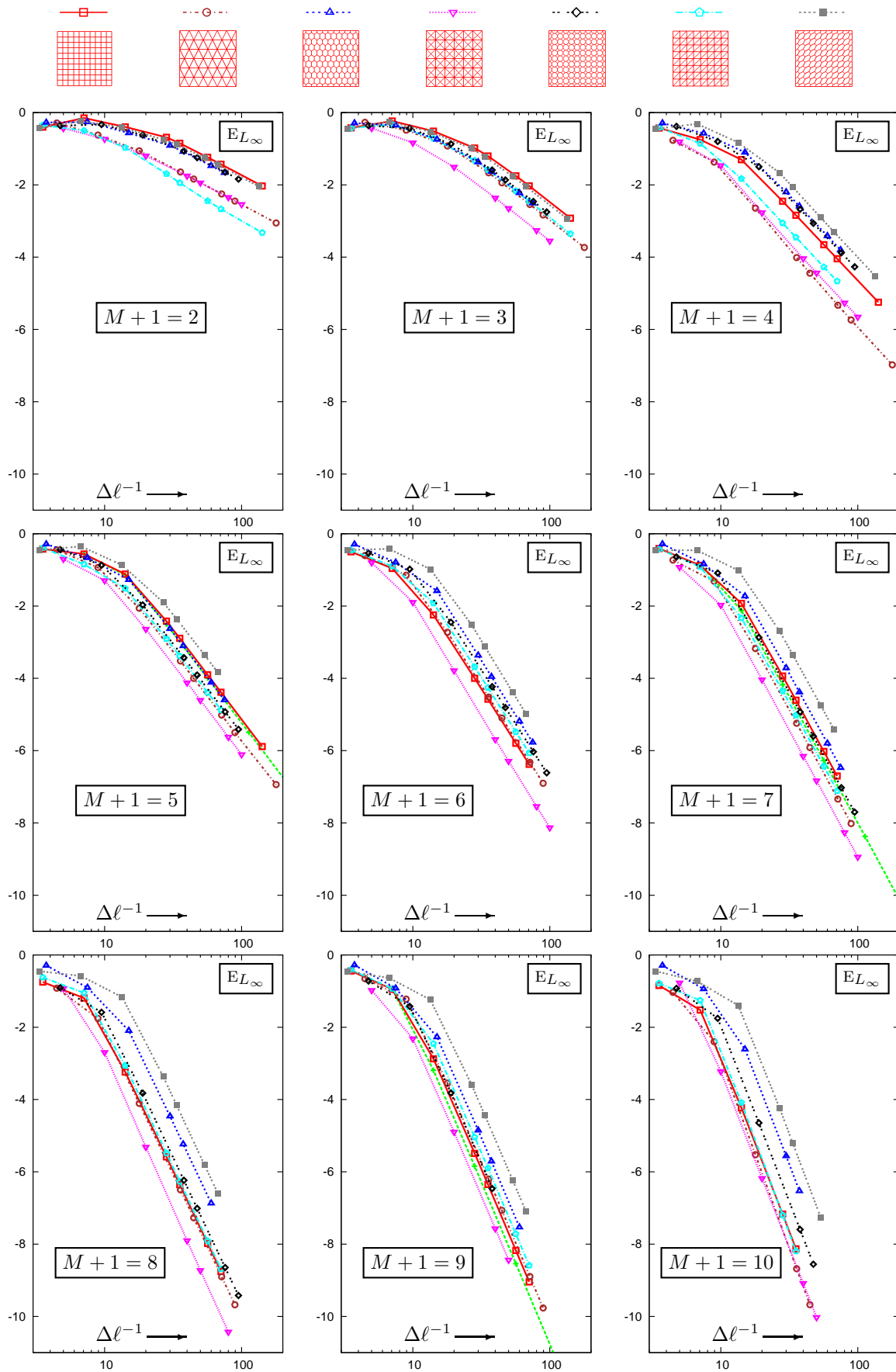
Figure 10: Comparison of the evolution of the error of the computations (Figs. 3–9) of the 2-D linear advection equation $\partial_t + \partial_x u + \partial_y u = 0$ ($x \in [-1, 1]$, $y \in [-1, 1]$), with periodic BCs, and IC $u_0(x) = \sin(\pi(x + y))$, between different types of grids (Fig. 1), for various orders ($M + 1 \in \{2, \cdots, 10\}$), as a function of grid-size $\Delta \ell$ (dotted green line with +, is the upwind-biased finite-difference solution on the corresponding Cartesian grid [14].
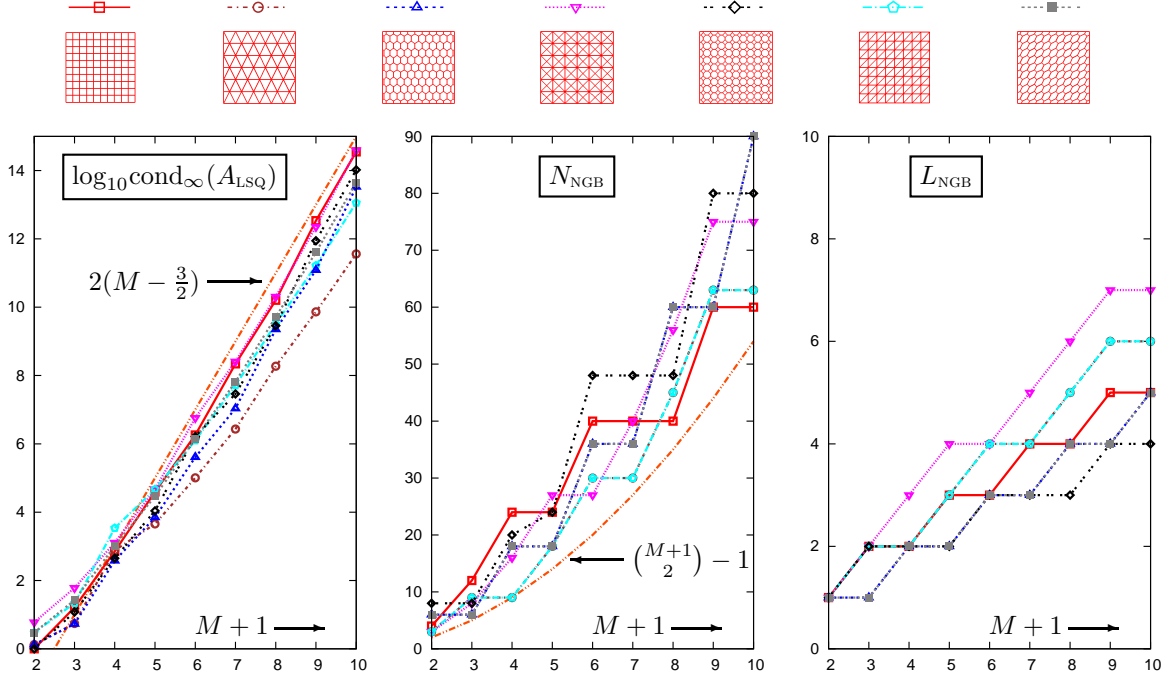
15

Figure 11: Evolution with order-of-accuracy $(M + 1)$, of the condition number of the reconstruction matrix $(\log_{10}\text{cond}_\infty A_{\text{LSQ}})$, of the number of neighbours in the stencil N_{NGB} and of the number of edge-neighbours levels of von Neumann neighbours used to construct the stencil L_{NGB}, for different types of regular polygonal grids.

4   Conclusion

In the present work we studied the order-of-accuracy of linear schemes on general unstructured meshes, The theoretical $O(\Delta\ell^{M+1})$-accuracy was always obtained for polynomial reconstruction degree M, but the level of the error for a given grid-size is sensitive to the computational grid (skew hexagonal grid being the worst).

Current work concentrates on representing the spectral accuracy of least-squares-reconstruction for different grids, developing a WENO reconstruction approach of scalable order on arbitrary grids (choice of substencils) and the evaluation of LSQ reconstruction for arbitrary curved polygons.

References

[1] K. W. Morton and T. Sonar. Finite volume methods for hyperbolic conservation laws. *Acta Num.*, 16:155–238, 2007.

[2] A. I. Delis, I. K. Nikolos, and M. Kazolea. Performance and comparison of cell-centered and node-centered unstructured finite-volume discretizations for the shallow water free surface flows. *Arch. Comp. Meth. Eng.*, 18:57–118, 2011.

[3] B. Diskin and J. L. Thomas. Comparison of node-centered and cell-centered unstructured finite volume discretiztions: Inviscid fluxes. *AIAA J.*, 49(4):836–854, April 2011.

[4] Q. Du, V. Faber, and M. Gunzburger. Centroidal voronoi tesselations: Applications and algorithms. *SIAM Rev.*, 41:637–676, 1999.

[5] C. Ollivier-Gooch. A toolkit for numerical simulation of pdes: I. fundamentals of generic finite-volume simulation. *Comp. Meth. Appl. Mech. Eng.*, 192:1147–1175, 2003.

[6] A. Harten, B. Engquist, S. Osher, and S. R. Chakravarthy. Uniformly high-order accurate essentially nonoscillatory schemes III. *J. Comp. Phys.*, 71:231–303, 1987.

[7] C. W. Shu. High-order WENO schemes for convection-dominated problems. *SIAM Rev.*, 51(1):82–126, February 2009.

[8] G. A. Gerolymos. Approximation error of the Lagrange reconstructing polynomial. *J. Approx. Theory*, 163(2):267–305, February 2011.

[9] L. Bos, J.-P. Calvi, N. Levenberg, A. Sommariva, and M. Vianello. Geometric weakly admissible meshes, discrete least squares approximations and approximate fekete points. *Math. Comp.*, 80(275):1623–1638, 2011.

[10] G. Santin, A. Sommariva, and M. Vianello. An algebraic cubature formula on curvilinear polygons. *Appl. Math. Comp.*, 217:10003–10015, 2011.

[11] D. A. Dunavant. High-degree efficient symmetrical Gaussian quadrature rules for the triangle. *Int. J. Num. Meth. Eng.*, 21:1129–1148, 1985.

[12] G. R. Cowper. Gaussian quadrature formuals for triangles. *Int. J. Num. Meth. Eng.*, 7:405–408, 1973.

[13] B. Van Leer. Upwind and high-resolution methods for compressible flow: From donor cell to residual distribution schemes. *Comm. Comp. Phys.*, 1(2):192–206, April 2006. (also AIAA Paper 2003–3559).

[14] G. A. Gerolymos, D. Sénéchal, and I. Vallet. Very-high-order WENO schemes. *J. Comp. Phys.*, 228:8481–8524, December 2009.

[15] S. Gottlieb. On high order strong stability preserving Runge-Kutta and multistep time discretizations. *J. Sci. Comp.*, 25(1):105–128, November 2005.